RESEARCH ARTICLE

NANO · MICRO small
www.small-journal.com

A Bismuth Surface Layer Enables Uniform Aluminum Electrodeposition for Reversible Aluminum Metal Anodes

*Yuxuan Zhu, Shunlong Ju, Long Yao, Guanglin Xia, and Xuebin Yu**

Metallic aluminum (Al) is an attractive anode material for Al-ion batteries owing to its high theoretical capacity and low cost. However, Al metal anodes suffer from surface passivation, dendrite growth, and parasitic reactions, hindering the practical applications of Al-ion batteries. Herein, a modified Al metal anode with a bismuth (Bi) artificial surface layer (Bi@Al) is developed by a facile in-situ substitution reaction method. The Bi layer accelerates the desolvation, nucleation, and Al^{3+} migration process, thereby facilitating homogeneous Al^{3+} distribution and rapid Al plating/stripping. Therefore, the modified Al metal anode achieves high reversibility and stability even under high current densities and capacities. As a result, Bi@Al symmetric cells exhibit a lifespan over 500 h at 10 mA cm^{-2} and 10 mAh cm^{-2}. Furthermore, combined with the graphite cathode, the Bi-modified Al metal full cell delivers a capacity of 80.1 mAh g^{-1} after 1000 cycles at 1.0 A g^{-1}. This work provides a valuable method to modify the Al metal anode for developing high-performance non-aqueous Al-ion batteries.

1. Introduction

Currently, the energy storage market is dominated by lithium-ion batteries (LIBs).[1] However, the further development of LIBs is restricted by safety concerns and the limited supply of lithium resources.[2,3] In search of alternatives to LIBs, battery systems based on monovalent (Na^+, K^+) or multivalent (Mg^{2+}, Al^{3+}, Ca^{2+}, and Zn^{2+}) metal ions have been extensively studied.[4–9] among these metal-based batteries, rechargeable Al-ion batteries (RABs) show promising prospects due to the high volumetric/gravimetric capacity (8056 mAh cm^{-3} and 2981 mAh g^{-1}, respectively), abundant resources, and attractive standard electrode potential (−1.66 V vs. standard hydrogen electrode).[10,11] However, RABs are still confronted with the inferior rate capacity and suboptimal cyclic stability.[10,12] Closely related to the difficulties faced by RABs, the durability of Al anodes presents a significant challenge, due to the dense oxide film on the surface of Al anodes which severely deteriorates the interface stability between anodes and electrolytes.[13,14] This passivation film is ionically and electrically insulating, resulting not only in an increased electrode potential but also in a slow Al plating/stripping process.[15] Furthermore, the oxide film is locally dissolved and recast as an unstable oxide interface during the electrochemical cycling, which leads to the growth of dendrites and low reversibility.[16,17] Therefore, precisely modulating the interfacial properties is essential for enhancing the kinetics and reversibility of Al plating/stripping processes, thereby facilitating improved electrochemical performance of RABs.[18]

Designing an appropriate surface layer to replace the natural oxide film is a critical approach for regulating deposition behavior and improving the cycling performance of Al metal anodes. For example, an MXene-based mixed ionic/electronic conductor interphase could homogenize the electric field distribution on the Al electrode surface.[19] A Pt-based ultrathin aluminophilic interface layer was constructed to achieve uniform nucleation and dendrite-free growth of Al metal deposition by reducing the energy barriers.[20] However, the stable cycling performance of Al anode at both high current densities and capacities remains challenging. Most previous works focus primarily on the Al deposition and growth processes at the anode surface, rather than on the interfacial interaction, such as the desolvation reaction, which also significantly affects the reaction kinetics and the distribution of Al^{3+}.[21] An inferior interfacial interaction may lead to increased voltage polarization and aggravated uneven Al deposition. Moreover, the synthesis procedures of the artificial interfaces reported previously are often too complex for large-scale applications.

Herein, we construct a new-type Al metal anode with a Bi surface layer (Bi@Al) through a facile in-situ substitution reaction between $BiCl_3$ and metallic Al. As indicated by density functional theory (DFT) calculations and various electrochemical measurements, the aluminophilic Bi layer accelerates the desolvation process and promotes the uniform distribution of Al^{3+}. Consequently, Bi@Al achieves homogeneous Al deposition and improves the electrochemical performance by constructing a stable anode-electrolyte interface. The symmetric cells based on Bi@Al electrodes exhibit a long-term cycle stability over 500 h with a low voltage hysteresis (<0.46 V) at 10 mA cm^{-2} and 10 mAh cm^{-2}. Moreover, the full cell, tested in combination of the Bi@Al anode and a graphite cathode demonstrate a specific capacity of 80.1 mAh g^{-1} after 1000 cycles at a current density of 1.0 A g^{-1}.

Y. Zhu, S. Ju, L. Yao, G. Xia, X. Yu
College of Smart Materials and Future Energy
Fudan University
Shanghai 200433, China
E-mail: yuxuebin@fudan.edu.cn

The ORCID identification number(s) for the author(s) of this article can be found under https://doi.org/10.1002/smll.202509150

DOI: 10.1002/smll.202509150

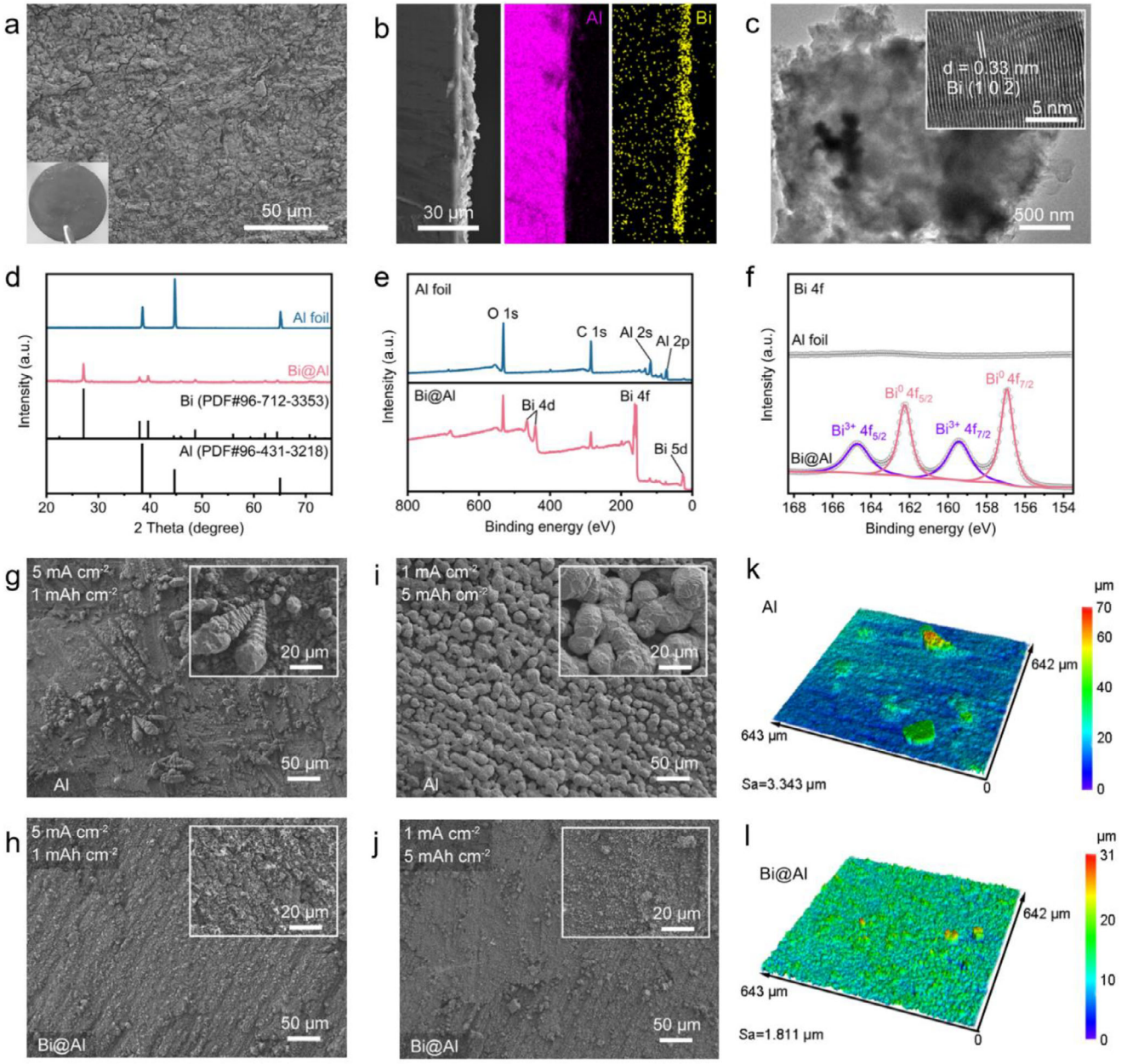

Figure 1. a) Surface SEM images of Bi@Al. b) Cross-sectional SEM images and corresponding elemental mapping images of Bi@Al. c) TEM images of the Bi layer. d) XRD patterns of Al foil and Bi layer. e) XPS spectra of Al and Bi@Al. f) Bi 4f XPS spectra of Al and Bi@Al. SEM images of g) Al, and h) Bi@Al after a deposition current density of 5 mA cm^{-2} and a capacity of 1 mAh cm^{-2}. SEM images of i) Al, and j) Bi@Al after a deposition current density of 1 mA cm^{-2} and a capacity of 5 mAh cm^{-2}. LSM images of k) Al, and l) Bi@Al after a deposition capacity of 3 mAh cm^{-2}.

2. Results and Discussion

In order to synthesize the Bi@Al electrode, the Al foil was immersed in 0.1 mol L^{-1} $BiCl_3$/DME solution for one minute until the black coating was formed in situ by a substitution reaction: $Al+BiCl_3 = AlCl_3+Bi$. The residues were then rinsed with pure DME. The surface scanning electron microscope (SEM) image in **Figure** 1a showed that an artificial surface layer with a textured structure was constructed on the surface of Al foil after the $BiCl_3$/DME solution treatment. Additionally, energy-dispersive spectroscopy (EDS) elemental mapping analysis illustrated a uniform distribution of the Bi element on the surface of Bi@Al (Figure S1, Supporting Information). The cross-sectional SEM image and corresponding EDS element mapping showed that Bi was concentrated in the surface layer, having a thickness of ≈5 μm (Figure 1b). To further verify the component of the surface layer, the black coating was scraped off from the surface of Bi@Al and the micromorphology was characterized by the transmission electron microscopy (TEM). The TEM images in Figure 1c revealed an interplanar spacing of 0.34 nm, corresponding to the Bi

(10$\bar{2}$) plane. X-ray diffraction (XRD) patterns in Figure 1d demonstrated that the diffraction peaks of Bi@Al matched well with metallic Bi. The strongest diffraction peak at 27.2° could be indexed to the (10$\bar{2}$) plane of metallic Bi, which was consistent with the TEM results. Compared to Al foil, Bi@Al exhibited much weaker characteristic diffraction peaks of metallic Al, indicating the dense coverage of the Bi surface layer. Because the native oxide film was amorphous, the XRD pattern of Al foil did not display any Al_2O_3 diffraction peak. However, the Al 2p X-ray photoelectron spectroscopy (XPS) spectrum confirms the presence of the oxide film (Figure S2, Supporting Information). Moreover, there were several characteristic peaks newly appeared in the XPS spectrum of Bi@Al, which could be assigned to Bi species (Figure 1e). Comparison of the Al 2p XPS spectra between Al and Bi@Al confirmed that the Bi surface layer effectively suppressed the formation of the oxide film (Figure S2, Supporting Information). In Figure 1f, the Bi 4f XPS spectrum of Bi@Al could be resolved into two components corresponding to Bi^0 (peaks at 156.9 and 162.2 eV) and Bi^{3+} (peaks at 159.4 and 164.7 eV). According to the above results, the Bi layer was formed on the surface of Al foil.

Ex situ XRD patterns of Bi@Al during Al plating showed the enhancement of the diffraction of metallic Al, indicating the occurrence of Al deposition (Figure S3, Supporting Information). The deposition morphology on Bi@Al and Al was observed by SEM. As shown in Figure 1g, when the deposition current density was 5 mA cm^{-2} with a capacity of 1 mAh cm^{-2}, sharp crystals were observed on the surface of Al. The dendrite growth would ultimately lead to internal short-circuiting of the battery. In contrast, small Al particles were deposited on the Bi without dendrites (Figure 1h). When the deposition capacity was increased from 1 to 5 mAh cm^{-2} with a fixed current density of 1 mA cm^{-2}, the surface morphology of Al exhibited spherical Al deposits which increased in size with the increase of capacities, indicating aggravated uneven deposition (Figure 1i; Figure S4, Supporting Information). Whereas Bi@Al achieved and remained uniform Al deposition as the increase of deposition capacity (Figure 1j; Figure S5, Supporting Information). Similar results were also observed in laser microscopy (LSM) images. After plating 3 mAh cm^{-2}, multiple Al particles were deposited on Al and the arithmetic mean height (S_a) of the test surface was 3.343 µm (Figure 1k). While Bi@Al exhibited a dendrites-free deposited surface and S_a value was 1.811 µm, which was lower than that of Al (Figure 1l). Cross-sectional SEM images in Figure S6 (Supporting Information) revealed that Bi@Al presented a more uniform and compact deposition morphology, in contrast to a loose and uneven deposition structure observed on the Al electrode. These results suggested that Bi@Al achieved uniform Al deposition under high current densities or capacities.

Electrochemical tests and DFT calculations were performed to further elucidate the role of the Bi layer in optimizing Al deposition. As revealed by cyclic voltammetry (CV) measurement in **Figure 2a**, Bi@Al displayed a higher peak current and a narrower voltage interval between oxidation and reduction peaks (0.33 V) than that of Al (0.46 V), indicating the reduced polarization and superior kinetics of Bi@Al.[22] Figure S7 (Supporting Information) presented the Tafel plots of Al and Bi@Al electrodes, from which the exchange current density of the Bi@Al was determined to be 0.764 mA cm^{-2}, exceeding that of the Al (0.182 mA cm^{-2}). This increase indicated superior reaction kinetics for Bi@Al, which contributed to enhanced cycling stability and improved rate capability. In addition, electrochemical impedance spectroscopy (EIS) measurements were conducted on Bi@Al and Al symmetric cells at different temperatures to evaluate the apparent activation energy (E_a) for desolvation kinetics (Figure S8, Supporting Information).[23] As shown in the Arrhenius plots in Figure 2b, the charge transfer resistance (R_{ct}) values of Bi@Al were lower than those of Al at each temperature. The derived E_a value for Bi@Al was 40.04 kJ mol^{-1}, lower than that for Al (52.69 kJ mol^{-1}). Furthermore, the R_{ct} of Bi@Al decreased significantly after cycling for 5 cycles and maintained a lower value compared to Al (Figure S9, Supporting Information). The reduced R_{ct} and E_a values of Bi@Al indicated a more favorable electrochemical reaction kinetics.

DFT calculations were then employed to provide deeper insight into the desolvation process. Because of the presence of a native oxide film on the Al surface, Al_2O_3 was selected as the substrate in the DFT calculations to realistically capture the interfacial environment and to clarify the role of the Bi surface layer in overcoming the limitations imposed by the oxide film. Based on the simulated adsorption configurations of Al^{3+} and chloroaluminate ions on Bi and Al_2O_3, the dissociation reactions of $Al_2Cl_7^-$ ions on Bi and Al_2O_3, where $Al_2Cl_7^-$ ions first decomposed into $AlCl_4^-$, then dissociated into $AlCl_2^+$, $AlCl^{2+}$, and ultimately Al^{3+}, were deciphered by DFT calculations (Figure S10, Supporting Information).[24] The Gibbs free energy profiles for the above four-step reactions were calculated and the results were shown in Figure 2c. The step involving the transformation of $AlCl_4^-$ to $AlCl_2^+$ exhibited the largest positive Gibbs free energy change (ΔG), it was thus identified as the rate-limiting step for the whole desolvation process. The ΔG value of Bi (2.71 eV) was smaller than that of Al_2O_3 (3.33 eV). This indicated that the desolvation process was more favorable on the Bi layer, which could be attributed to the destabilization of the Al-Cl bond induced by Bi. These results agreed with the experimental findings and confirmed that the Bi layer reduced the interfacial resistance at the electrode surface and enhanced the kinetics of the desolvation process.

Figure 2d displays the overpotential during the nucleation process under 1 mA cm^{-2}. The nucleation overpotential of Bi@Al was 46.6 mV, which was significantly lower than that of Al (119.2 mV). Notably, Bi@Al consistently exhibited a lower nucleation overpotential across a range of current densities from 1 to 5 mA cm^{-2}, which substantiated the enhanced aluminophilicity of the Bi surface layer (Figure 2e; Figure S11, Supporting Information). DFT calculations further elucidated the favorability of Al deposition on Bi. The charge density difference maps for Al^{3+} on Al_2O_3 and Bi substrates are shown in Figure 2f,g and there are larger and more continuous positive isosurfaces for Al^{3+} on Bi than Al. This showed a stronger interface coupling between Al^{3+} and Bi, suggesting a higher Al affinity of the Bi layer.

In addition, as listed in Figure 2h, the binding energies (E_b) of Al^{3+} and chloroaluminate ions on Bi were all lower than those on Al_2O_3, indicating a stronger affinity of Bi substrate for both Al^{3+} and chloroaluminate ions in the electrolytes. This not only enabled sufficient interfacial contact between the Bi substrate and chloroaluminate ions for effective catalysis, but also promoted adsorption and homogeneous nucleation of Al^{3+}. Specifically, Bi

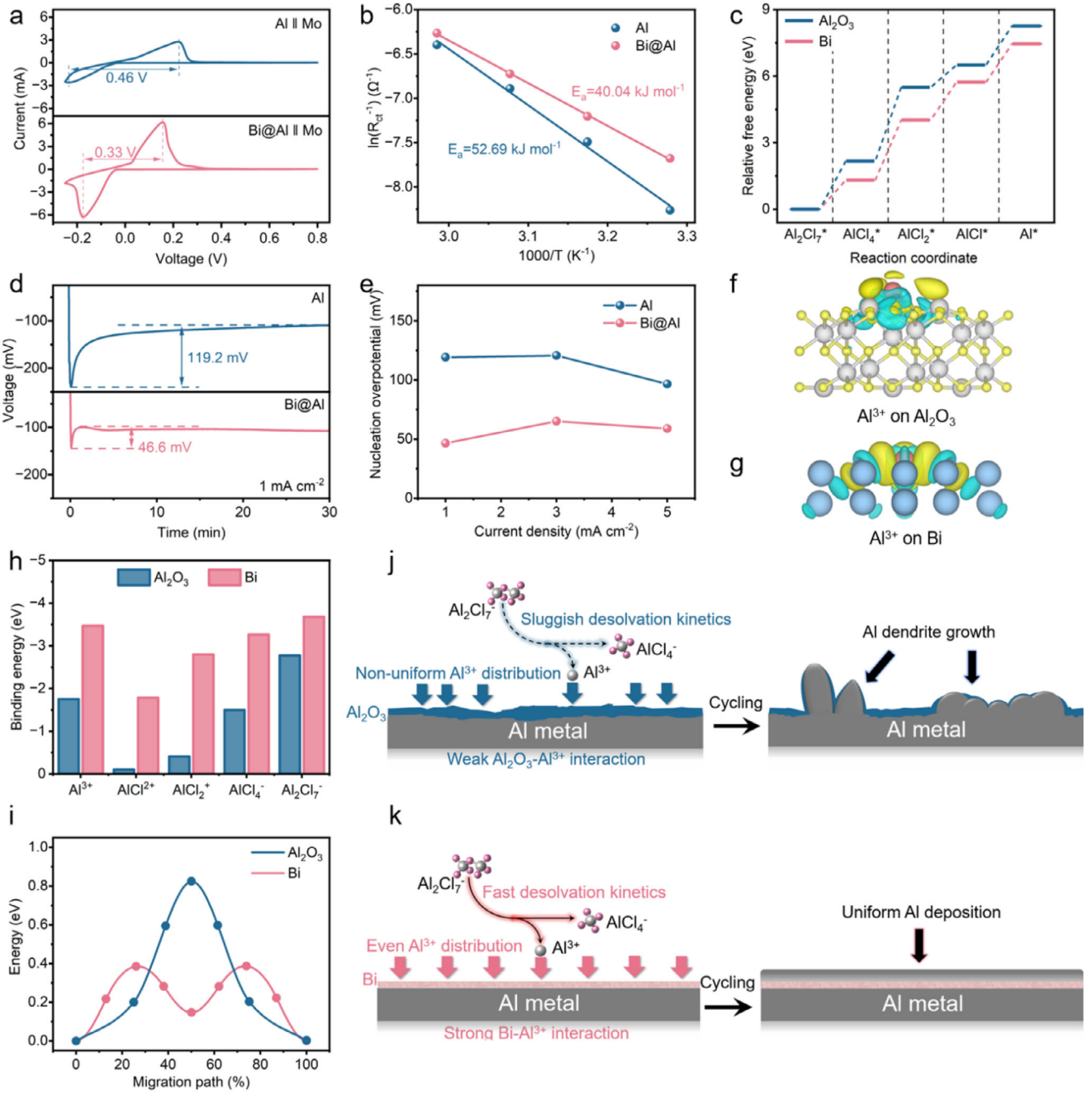

Figure 2. a) CV curves of Al//Mo and Bi@Al//Mo cells at a scan rate of 2 mV s^{-1}. b) Arrhenius plots of Al and Bi@Al symmetric cells. c) Relative free energy profiles for the desolvation process of $Al_2Cl_7^-$ on Bi and Al_2O_3. Energies were normalized against the energy of the $Al_2Cl_7^-$ ion on Bi and Al_2O_3 substrates, respectively. d) Voltage profiles for the initial Al deposition on Al and Bi@Al at 1 mA cm^{-2}. e) Nucleation overpotentials of Al and Bi@Al at different current densities. Charge density difference maps for Al^{3+} on f) Al_2O_3 and g) Bi substrates. h) Binding energies of $Al_2Cl_7^-$, $AlCl_4^-$, $AlCl_2^+$, $AlCl^{2+}$, Al^{3+} on Bi and Al_2O_3. i) The energy profile corresponding to the migration process of Al^{3+} ion on Bi and Al_2O_3. Schematic illustration of the Al deposition behavior at the surface of j) Al and k) Bi@Al.

exhibited a significantly smaller E_b value for Al^{3+} (−3.47 eV) than Al_2O_3 (−1.75 eV). The results of DFT calculations coincided with the conclusions drawn from electrochemical tests and demonstrated the efficacy of the Bi layer in reducing Al nucleation barrier, which was conducive to a more homogeneous Al deposition. Furthermore, energy profiles for Al^{3+} migration on Bi and Al_2O_3 substrates were obtained by optimizing adsorption configurations at various sites (Figure S12, Supporting Information). As shown in Figure 2i, there was a high Al^{3+} diffusion energy barrier along the migration path on the Al_2O_3 substrate (0.83 eV), whereas there was lower energy barrier on the Bi substrate (0.38 eV). The reduced diffusion energy barriers facilitate

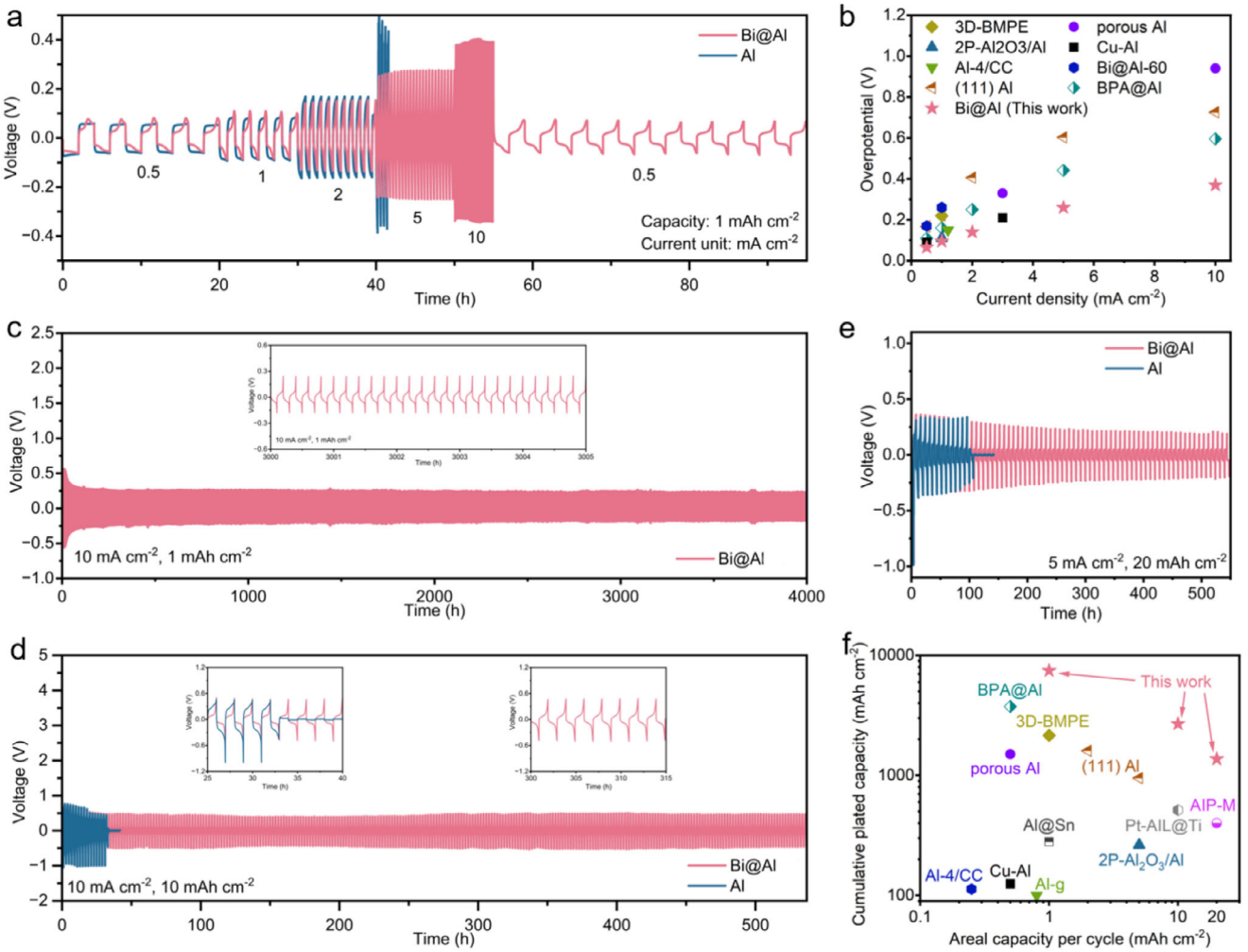

Figure 3. a) Rate performance of Al and Bi@Al symmetric cells. b) Comparison of the overpotentials of Bi@Al anode with reported modified Al anodes. c) Long-term cycling performance of Bi@Al symmetric cell at 10 mA cm^{-2} and 1 mAh cm^{-2}. Cycling performance of Al and Bi@Al symmetric cells at d) 10 mA cm^{-2} and 10 mAh cm^{-2}, e) 5 mA cm^{-2} and 20 mAh cm^{-2}. f) Comparison of the cycling performance of Bi@Al anode with reported modified Al anodes.

uniform distribution of Al^{3+}. The above-mentioned characteristics of the Bi layer reduced the nucleation overpotentials and enabled homogeneous Al deposition, aligning with the results of morphological observations.

According to the aforementioned characteristics of Bi@Al, such as low nucleation overpotential and enhanced kinetics, the working mechanism of Bi@Al in suppressing dendrite growth and facilitating uniform Al deposition was proposed (Figure 2j,k). The Bi layer exhibited multiple important functions including reducing the nucleation barriers, promoting the even distribution of Al^{3+} and accelerating the dissociation process of $Al_2Cl_7^-$, thereby enabling uniform Al deposition under high current densities or capacities.

The electrochemical performance of Bi@Al symmetric cells was tested to verify the effect of the Bi layer in rate capability and cyclic stability. In **Figure 3a**, Bi@Al symmetric cell demonstrated stable and low voltage hysteresis over the current density range from 0.5 to 10 mA cm^{-2} and the voltage curves returned to the previous state when the current density was reduced to 1 mA cm^{-2}, indicating the superior rate performance of Bi@Al. In contrast, symmetric cell using Al electrodes experienced a short circuit when the current density was increased to 5 mA cm^{-2}, probably due to dendrite growth at high current densities. Figure 3b and Table S1 (Supporting Information) compare the overpotential of Bi@Al with several previously reported Al metal anodes.[12,25–31] It could be seen that Bi@Al exhibits a lower overpotential, especially at high current densities, compared to these reported anodes.

When the current density was maintained at 10 mA cm^{-2}, the maximum in the rate performance measurement, Bi@Al still exhibited a stable voltage profile with a low voltage hysteresis (<0.23 V) and ultralong lifespan over 4000 h (Figure 3c). Notably, when the deposition capacity was increased to 10 mAh cm^{-2} with a fixed current density of 10 mA cm^{-2}, Bi@Al symmetric cell still showed high reversibility with a lifespan exceeding 500 h (Figure 3d), highlighting the improved electrochemical performance due to the Bi layer in accelerating desolvation and suppressing the formation of Al dendrites. Even under a

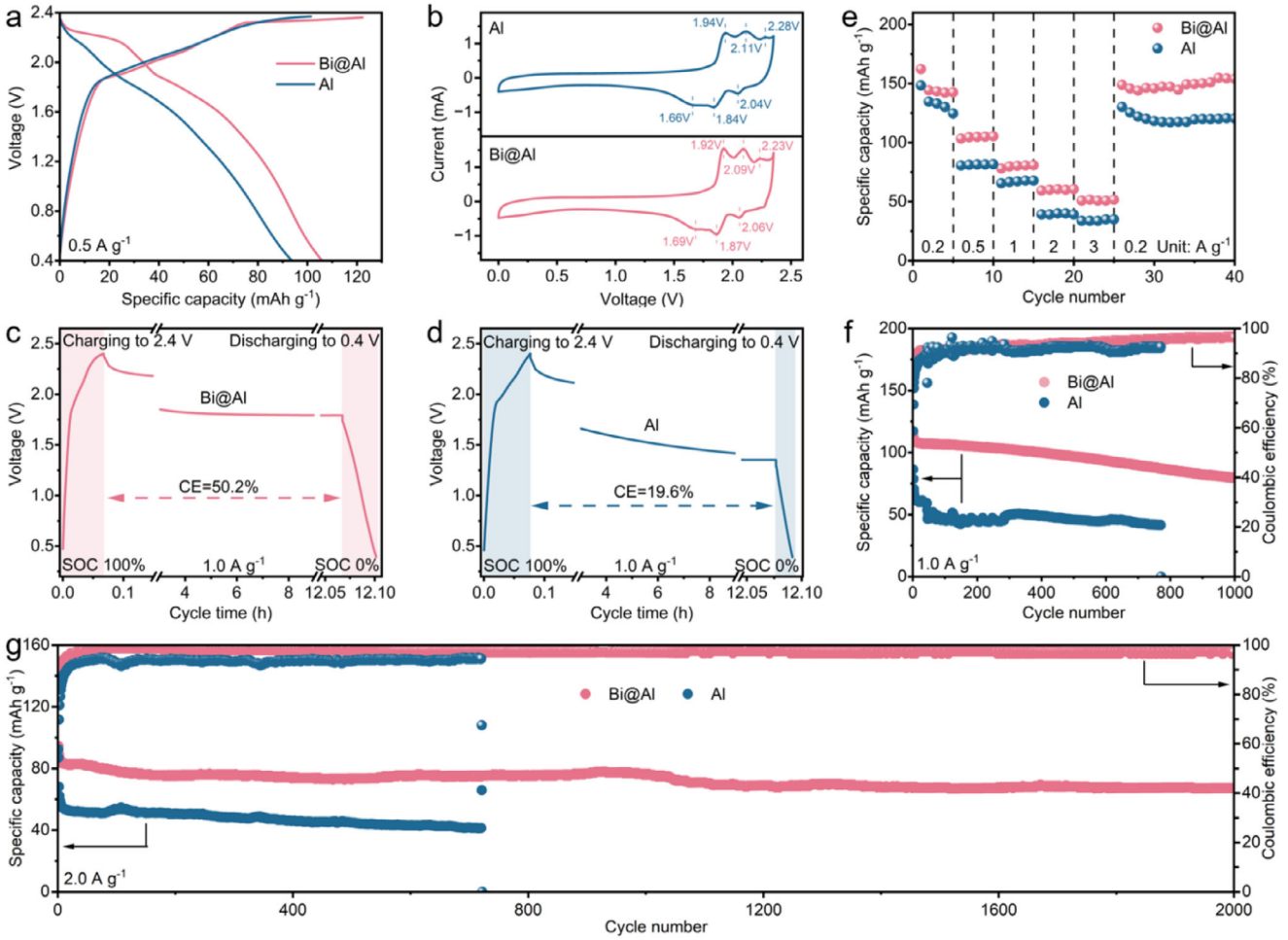

Figure 4. a) Galvanostatic charge/discharge profiles of Al//graphite and Bi@Al//graphite full cells at 0.5 A g^{-1}. b) CV curves of Al//graphite and Bi@Al//graphite full cells at a scan rate of 2 mV s^{-1}. c) Bi@Al//graphite and d) Al//graphite full cells were first fully charged to 2.4 V at 1.0 A g^{-1}, and then rested for 12 h, followed by full discharging to 0.4 V. e) Rate performance of Al//graphite and Bi@Al//graphite full cells at current densities from 0.2 to 3 A g^{-1}. Cycling performance of Al//graphite and Bi@Al//graphite full cells at f) 1.0 A g^{-1}, and g) 2.0 A g^{-1}.

higher deposition capacity (5 mA cm^{-2}, 20 mAh cm^{-2}) or current density (40 mA cm^{-2}, 1 mAh cm^{-2}), Bi@Al symmetric cells maintained stable cycling for hundreds of hours (Figure 3e; Figure S13, Supporting Information). In contrast, Al symmetric cells short-circuited rapidly under such extreme conditions due to dendrites formation. Figure 3f and Table S2 (Supporting Information) present a comparison of the electrochemical performance of Bi@Al with previously reported anodes.[12,16,20,25–32] The cumulative plated capacity was obtained by multiplying the current density with the cycling time of Al plating. As shown, these advancements contributed to the high cumulative capacity up to 20 mAh cm^{-2}, demonstrating the superior electrochemical performance of Bi@Al in terms of stability and rate capability under high current densities and capacities.

To investigate the availability of the Bi@Al anode, Al-ion full cells were assembled by pairing graphite cathode with Bi@Al and Al anodes (denoted as Bi@Al//graphite and Al//graphite) for electrochemical measurements. As shown in the galvanostatic charge/discharge curves in **Figure 4a**, Bi@Al//graphite exhibited a higher discharge plateau and specific capacity compared to the Al//graphite. The charge/discharge profiles over cycles showed that Bi@Al//graphite exhibited stable voltage plateaus and minimal capacity decrease, in contrast to the significant capacity decay and increased polarization observed for the Al//graphite, indicating the strong cycling stability of Bi@Al (Figure S14, Supporting Information). Meanwhile, CV curves in Figure 4b revealed that Bi@Al//graphite demonstrated a higher peak current and a narrower voltage gap between redox peaks, indicating a faster redox kinetics and better redox reversibility. In the EIS spectra in Figure S15 (Supporting Information), Bi@Al//graphite cell showed a lower R_{ct} than Al//graphite, which confirmed that the enhancement of kinetics by Bi@Al anode. EIS spectra after different cycles further revealed that Bi@Al//graphite maintained stable interfacial resistance during cycling, whereas Al//graphite showed a progressive increase in R_{ct} (Figure S16, Supporting Information).

Furthermore, the effectiveness of the Bi layer in suppressing parasitic reactions in Bi@Al//graphite cell was evaluated by monitoring the open circuit voltage decay of a fully charged cell, followed by discharging it to 0.4 V after a 12 h of storage.

Bi@Al//graphite retained 50.2% of its initial capacity (Figure 4c), which was much better than Al//graphite (19.6% retention in Figure 4d). The rate performances of these full cells were shown in Figure 4e. Bi@Al//graphite exhibited higher specific capacities across various current densities compared to Al//graphite. Specially, Bi@Al//graphite maintained a specific capacity of 51.8 mAh g^{-1} at a high current density of 3 A g^{-1}, and the specific capacity recovered to its initial level when the current density was returned to 0.2 A g^{-1}. Figure 4f,g demonstrate the cycling performance of the full cells. At 1.0 A g^{-1}, Bi@Al//graphite cell retained a specific capacity of 80.1 mAh g^{-1} after 1000 cycles with a coulombic efficiency (CE) of 96.9%. In contrast, the specific capacity of Al//graphite cell rapidly declined in the initial cycles, and the cell failed after 770 cycles (Figure 4f). After cycling, the Bi@Al electrode maintained a surface structure comparable to that prior to the electrochemical test, which contributed to the long-term stability of Bi@Al (Figure S17, Supporting Information). When the current density was increased to 2.0 A g^{-1}, Bi@Al//graphite cell retained a specific capacity of 67.2 mAh g^{-1} after 2000 cycles, with a CE of 97.3% (Figure 4g). These results further highlighted the high reversibility and stability of the Bi@Al anode.

3. Conclusion

In summary, we constructed a modified Al metal anode with a Bi surface layer by a simple substitution reaction. Bi@Al anode enabled smooth and dendrite-free Al deposition morphology, attributed to the aluminophilic Bi layer accelerating the desolvation process and enabling homogeneous Al^{3+} distribution. As expected, the Bi@Al symmetric cell achieved stable cycles for over 500 h at 10 mA cm^{-2} and 10 mAh cm^{-2}. Moreover, the Bi@Al//graphite full cells delivered remarkably improved cycle reversibility and stability. After 2000 cycles at a current density of 2.0 A g^{-1}, the Bi@Al//graphite full cell showed a specific capacity of 67.2 mAh g^{-1}. This work provides a simple method to modify the Al metal anode surface and construct high-performance RABs.

4. Experimental Section

Preparation of Anode: The surface of the Al foil was polished with sandpaper to remove the oxide layer. Typically, 0.315 g $BiCl_3$ (99.99%, Aladdin) were dissolved in 10 mL 1,2-dimethoxyethane (DME, 99.5%, Aladdin) to prepare a 0.1 mol L^{-1} $BiCl_3$/DME solution. Then the Al foil was soaked in 0.1 mol L^{-1} $BiCl_3$/DME for one minute. Finally, the residues were washed away with pure DME to obtain the Bi@Al anode. The preparation process was carried out in an argon atmosphere glovebox with less than 0.1 ppm of H_2O and O_2.

Preparation of Cathode: Commercial graphite, carbon black, and polyvinylidene difluoride (PVDF, HSV900, Arkema) were dispersed in 1-methyl-2-pyrrolidinone (NMP, C_5H_9NO, 99.5%, Aladdin) at a mass ratio of 7:2:1. The resulting homogeneous slurry was coated onto Mo foil and dried at 70 °C for 12 h in a vacuum oven to prepare graphite cathode. The mass loading of active materials at each electrode was ≈1.2 mg cm^{-2}.

Preparation of Ionic Liquid Electrolytes: $AlCl_3$ (99%, Aladdin) and 1-ethyl-methylimidazolium chloride ([EMIm]Cl, 98%, Aladdin) were mixed at a molar ratio of 1.3:1 and continuously stirred in an Argon atmosphere glovebox. The obtained light-yellow electrolyte was held in the glovebox for 12 h for standby.

Batteries Assembly: AIBs were assembled in Swagelok-type cells with glass fiber separators and as-prepared ionic liquid electrolytes. The amount of electrolyte used in cell assembly was 120 µL cm^{-2}. Symmetric cells were fabricated using identical electrodes of either pure Al or Bi@Al. The asymmetric cells were constructed by substituting one of the electrodes with a molybdenum (Mo) foil. Al-ion full batteries were assembled by using pure Al or Bi@Al as anodes and the graphite cathode. All batteries were assembled in an Ar-filled glovebox and aged for 12 h before performing electrochemical measurements.

Material Characterizations: The morphology and microstructural features of the samples were analyzed by the laser microscope (OLS5000), the scanning electron microscopy (JEOL 7500FA) equipped with energy dispersive X-ray spectroscopy, and the transmission electron microscope (JEOL JEM-F200). X-ray diffractometer (Bruker D8 Advance) with monochromatic Cu K_α as the radiation source was employed to investigate the lattice structure of samples. Additionally, the chemical compositions of the samples were examined by X-ray photoelectron spectroscopy (Thermo Scientific K-Alpha).

Electrochemical Measurement: Galvanostatic cycling tests were carried out on a NEWARE CT-4008T battery testing system. Cyclic voltammetry (CV), linear sweep voltammetry (LSV), and electrochemical impedance spectroscopy (EIS) were conducted on a VMP3 multi-channel electrochemical workstation (BioLogic SP-300). CV tests were conducted within the voltage window of 0 to 2.4 V (for full cells) and −0.25 to 0.8 V (for asymmetric cells) at a fixed scanning speed of 2 mV s^{-1}. LSV tests were conducted the voltage window of -2.5 to 2.5 V at 1 mV s^{-1}. EIS measurements covered frequencies ranging from 100 kHz to 10 mHz. The charge-transfer resistance (R_{ct}) of various test cells at different temperatures was evaluated based on the EIS spectra by fitting the equivalent circuit model. The desolvation activation energy (E_a) could be quantitatively calculated according to the following Arrhenius equation:

$$\frac{1}{R_{ct}} = A exp\left(-\frac{E_a}{RT}\right) \quad (1)$$

where the *A*, *R*, and *T* stand for the frequency factor, the ideal gas constant, and the temperature in Kelvin, respectively.

Computational Methods: First-principles computations based on density functional theory (DFT) were conducted to characterize the system's electronic properties. The simulations adopted the projector-augmented wave (PAW) method as implemented in Vienna ab initio simulation package (VASP). For the electron exchange-correlation, generalized gradient approximation (GGA) of Perdew-Burke-Ernzerhof (PBE) functional was implemented, complemented by the van der Waals (vdW) correction DFT-D3 proposed by Grimme, which was used to describe the dispersion interaction. A plane-wave basis set cutoff of 500 eV and Γ-centered k-point grids with the same sampling density were applied to surface calculations. Spin polarization was considered, and Gaussian broadening with 0.05 eV was used in electronic structure calculations. Structural optimization proceeded until atomic forces and total energy differentials were converged to less than 0.05 eV $Å^{-1}$ and 1×10^{-5} eV respectively. The adsorption energetics of aluminum on different surfaces were quantified through binding energy (E_b) calculations:

$$E_b = E_b - (E_{Al} + E_{substrate}) \quad (2)$$

In this formulation, E_{total} signifies the total energy of the Al-absorbed system. $E_{substrate}$ indicates the energy of the pristine surface without deposition. E_{Al} reflects the per-atom bulk aluminum energy. The thermodynamically favorable nature of Al deposition is signaled by negative E_b values, where increasingly negative values correlate with enhanced bonding stability at the material interface. The relative free energy of the desolvation process of $Al_2Cl_7^-$ was calculated following the reaction sequence of:

$$Al_2Cl_7^- \xrightarrow{I} AlCl_4^- \xrightarrow{II} AlCl_2^+ \xrightarrow{III} AlCl^{2+} \xrightarrow{IV} Al^{3+} \quad (3)$$

The corresponding reaction energies for these four steps were calculated using the following equations:

$$E_I = E_{AlCl_4+substrate} + E_{AlCl_3} - E_{Al_2Cl_7+substrate} \quad (4)$$

$$E_{II} = E_{AlCl_2+substrate} + 2E_{Cl} - E_{AlCl_4+substrate} \quad (5)$$

$$E_{III} = E_{AlCl+substrate} + E_{Cl} - E_{AlCl_2+substrate} \quad (6)$$

$$E_{IV} = E_{Al+substrate} + E_{Cl} - E_{AlCl+substrate} \quad (7)$$

where E_{Cl} is the energy of Cl atom and E_{AlCl_3} is the energy of $AlCl_3$ cluster.

Supporting Information

Supporting Information is available from the Wiley Online Library or from the author.

Acknowledgements

Y.Z. and S.J. contributed equally to this work. This work was partially supported by the National Key R&D Program of China (2023YFB2504000), the National Natural Science Foundation of China (52501274), the Innovation Program of Shanghai Municipal Education Commission (2025GDZKZD01), and the China Postdoctoral Science Foundation (2023M740639).

Conflict of Interest

The authors declare no conflict of interest.

Data Availability Statement

The data that support the findings of this study are available from the corresponding author upon reasonable request.

Keywords

aluminum metal anode, aluminum-ion batteries, bismuth, dendrite growth, desolvation

Received: July 30, 2025
Revised: September 11, 2025
Published online: October 3, 2025

[1] B. Dunn, H. Kamath, J.-M. Tarascon, *Science* **2011**, *334*, 928.
[2] J. B. Goodenough, K.-S. Park, *J. Am. Chem. Soc.* **2013**, *135*, 1167.
[3] Y. Zhou, C.-H. Wang, W. Lu, L. Dai, *Adv. Mater.* **2020**, *32*, 2070037.
[4] H. Kim, J. Hong, K.-Y. Park, H. Kim, S.-W. Kim, K. Kang, *Chem. Rev.* **2014**, *114*, 11788.
[5] Y.-Q. Li, H. Shi, S.-B. Wang, Y.-T. Zhou, Z. Wen, X.-Y. Lang, Q. Jiang, *Nat. Commun.* **2019**, *10*, 4292.
[6] Z. H. Song, Z. H. Zhang, A. B. Du, S. M. Dong, G. C. Li, G. L. Cui, *Adv. Mater.* **2021**, *33*, 2100224.
[7] H. Wang, L. Zhao, H. Zhang, Y. Liu, L. Yang, F. Li, W. Liu, X. Dong, X. Li, Z. Li, X. Qi, L. Wu, Y. Xu, Y. Wang, K. Wang, H. Yang, Q. Li, S. Yan, X. Zhang, F. Li, H. Li, *Energy Environ. Sci.* **2022**, *15*, 311.
[8] X. Tang, D. Zhou, B. Zhang, S. Wang, P. Li, H. Liu, X. Guo, P. Jaumaux, X. Gao, Y. Fu, C. Wang, C. Wang, G. Wang, *Nat. Commun.* **2021**, *12*, 2857.
[9] N. N. Zhang, S. Huang, Z. S. Yuan, J. C. Zhu, Z. F. Zhao, Z. Q. Niu, *Angew. Chem. Int. Ed.* **2021**, *60*, 2861.
[10] M. Jiang, C. Fu, P. Meng, J. Ren, J. Wang, J. Bu, A. Dong, J. Zhang, W. Xiao, B. Sun, *Adv. Mater.* **2022**, *34*, 2102026.
[11] K. L. Ng, B. Amrithraj, G. Azimi, *Joule* **2022**, *6*, 134.
[12] Y. Long, H. Li, M. Ye, Z. Chen, Z. Wang, Y. Tao, Z. Weng, S.-Z. Qiao, Q.-H. Yang, *Energy Storage Mater.* **2021**, *34*, 194.
[13] X. T. Wang, Z. H. Xi, Q. Zhao, *Ind. Chem. Mater.* **2025**, *3*, 7.
[14] Q. Ran, H. Shi, H. Meng, *Nat. Commun.* **2022**, *13*, 576.
[15] S. Choi, H. Go, G. Lee, Y. Tak, *Phys. Chem. Chem. Phys.* **2017**, *19*, 8653.
[16] C. Xie, F. Wu, Z. Lv, Y. Zhang, Y. Mei, W. Ma, W. Sun, J. Zhou, M. Xie, *Adv. Funct. Mater.* **2024**, *34*, 2408296.
[17] J. Zheng, D. C. Bock, T. Tang, Q. Zhao, J. Yin, K. R. Tallman, G. Wheeler, X. Liu, Y. Deng, S. Jin, A. C. Marschilok, E. S. Takeuchi, K. J. Takeuchi, L. A. Archer, *Nat. Energy* **2021**, *6*, 398.
[18] Q. Ran, S. P. Zeng, M. H. Zhu, *Adv. Funct. Mater.* **2023**, *33*, 2211271.
[19] L. Yao, S. L. Ju, T. Xu, W. B. Wang, Yu, *ACS Nano* **2023**, *17*, 25027.
[20] Y. Meng, M. Wang, K. Li, Z. Zhu, Z. Liu, T. Jiang, X. Zheng, K. Zhang, W. Wang, Q. Peng, Z. Xie, Y. Wang, W. Chen, *Nano Lett.* **2023**, *23*, 2295.
[21] S. Chen, J. Chen, X. Liao, Y. Li, W. Wang, R. Huang, T. Zhao, S. Yan, Z. Yan, F. Cheng, H. Wang, *ACS Energy Lett.* **2022**, *7*, 4028.
[22] J. Bi, Y. Liu, Z. Du, K. Wang, W. Guan, H. Wu, W. Ai, W. Huang, *Adv. Mater.* **2024**, *36*, 2309339.
[23] H. Yu, Y. Chen, W. Wei, X. Ji, L. Chen, *ACS Nano* **2022**, *16*, 9736.
[24] Z. Huang, W. Wang, W.-L. Song, M. Wang, H. Chen, S. Jiao, D. Fang, *Angew. Chem., Int. Ed.* **2022**, *134*, 202202696.
[25] H. Jiao, S. Jiao, W.-L. Song, H. Chen, M. Wang, J. Tu, D. Fang, *J. Electrochem. Soc.* **2019**, *166*, A3539.
[26] J. Li, K. S. Hui, S. Ji, C. Zha, C. Yuan, S. Wu, F. Bin, X. Fan, F. Chen, Z. Shao, K. N. Hui, *Carbon Energy* **2022**, *4*, 155.
[27] S. Wang, Y. Guo, X. Du, L. Xiong, Z. Huang, X. Li, Y. Xie, M. Ma, Z. Liang, *Nano Energy* **2023**, *114*, 108626.
[28] S. He, J. Wang, X. Zhang, W. Chu, S. Zhao, D. He, M. Zhu, H. Yu, *J. Mater. Chem. A* **2023**, *11*, 17020.
[29] Y. H. Heo, J. Lee, S. Ha, J. Chan Hyun, D. H. Kang, J. Yoon, H. S. Kim, Y. Choi, Y. Chan Kang, H.-J. Jin, S. J. Kim, Y. S. Yun, *J. Mater. Chem. A* **2023**, *11*, 14380.
[30] S. Wang, Y. Guo, X. Du, Z. Liang, M. Ma, Y. Xie, W. You, Y. Meng, D. Li, M. Liu, Y. Liu, *Chem. Eng. J.* **2024**, *494*, 153194.
[31] S. Wang, Y. Guo, X. Du, L. Xiong, Z. Liang, M. Ma, Y. Xie, W. You, Y. Meng, Y. Liu, M. Liu, *Nat. Commun.* **2024**, *15*, 6476.
[32] D. Li, Y. Liu, Y. Xie, X. Wang, D. He, P. Wang, L. Xiong, *J. Power Sources* **2025**, *641*, 236860.